---

**Article:**
Ferreira, Aires orcid.org/0000-0001-6017-8669 (2021) Theory of spin–charge-coupled transport in proximitized graphene: an SO(5) algebraic approach. Journal of Physics: Materials. 045006. ISSN: 2515-7639

https://doi.org/10.1088/2515-7639/ac31b5

---

# Theory of spin–charge-coupled transport in proximitized graphene: an SO(5) algebraic approach

IOP Publishing J. Phys. Mater. 4 (2021) 045006 https://doi.org/10.1088/2515-7639/ac31b5

Journal of Physics: Materials

OPEN ACCESS

RECEIVED
31 July 2021

ACCEPTED FOR PUBLICATION
20 October 2021

PUBLISHED
28 October 2021



PAPER

# Theory of spin–charge-coupled transport in proximitized graphene: an SO(5) algebraic approach

Aires Ferreira

Department of Physics and York Centre for Quantum Technologies, University of York, York, YO10 5DD, United Kingdom

**E-mail:** aires.ferreira@york.ac.uk

**Keywords:** spintronics, spin-orbit coupling, graphene, van der Waals heterostructures, spin-charge conversion, spin dynamics

## Abstract

Establishing the conditions under which orbital, spin and lattice-pseudospin degrees of freedom are mutually coupled in realistic nonequilibrium conditions is a major goal in the emergent field of graphene spintronics. Here, we use linear-response theory to obtain a unified microscopic description of spin dynamics and coupled spin–charge transport in graphene with an interface-induced Bychkov–Rashba effect. Our method makes use of an SO(5) extension of the familiar inverse-diffuson approach to obtain a quantum kinetic equation for the single-particle density matrix that treats spin and pseudospin on equal footing and is valid for arbitrary external perturbations. As an application of the formalism, we derive a complete set of drift–diffusion equations for proximitized graphene with scalar impurities in the presence of electric and spin-injection fields which vary slowly in space and time. Our approach is amenable to a wide variety of generalizations, including the study of coupled spin–charge dynamics in layered materials with strong spin–valley coupling and spin–orbit torques in van der Waals heterostructures.

## 1. Introduction

There is a current fundamental and technological interest in the harnessing of spin–orbit-coupling (SOC) effects in nonmagnetic media, particularly for the interconversion of charge and spin currents and the generation of nonequilibrium spin polarization [1, 2]. A recent trend is the use of two-dimensional (2D) materials to engender electrical control over SOC effects benefiting from their reduced dimensionality and unique opto-electronic properties afforded by atomically thin crystals and their heterostructures [3, 4]. With graphene well established as a high-fidelity spin channel material supporting room-temperature spin transport over lengths up to tens of micrometers [5–10], an important challenge concerns the manipulation of nonequilibrium spins by pure electrical means for future spin-logic applications. While at first glance this might seem hopeless given the absence of bulk ferromagnetism in graphene [11], not to mention its ultra-low intrinsic SOC [12], several strategies have been proposed to overcome this bottle neck, including adatom engineering [13, 14] and proximity effects achieved via van der Waals coupling to high-SOC 2D materials [15–19]. The latter approach has shown great promise because the proximity-induced SOC can be well resolved in energy (i.e. on the order of the quasiparticle broadening), which facilitates the experimental demonstration of SOC effects with reproducibility, e.g. by means of low-field magnetotransport measurements [20–24]. Furthermore, the strong interplay of spin and lattice-pseudospin degrees of freedom in honeycomb layered materials gives rise to fingerprints of unique hallmarks of SOC in spin transport experiments. Most notably, the emergence of spin–helical 2D Dirac fermions in van der Waals heterostructures due to the Bychkov–Rashba (BR) effect [25] has been predicted [26] and demonstrated experimentally [27–30] to enable efficient spin–charge interconversion at room temperature. Owing to a unique spin–pseudospin entanglement of electronic wavefunctions, the sign and magnitude of the nonequilibrium spin polarization in BR-coupled graphene can be tuned with a back-gate voltage [26], in contrast to spin-galvanic effects generated by topological insulators [31]. Another interesting manifestation of proximity-induced SOC is observed in Hanle-type spin precession experiments [32, 33], where a rather unconventional spin dynamics results in spins polarized in the plane of graphene relaxing about ten times

faster than out-of-plane spins. This effect, originally predicted by Cummings and co-workers [34], is explained by the combined action of interface-induced spin–valley coupling and intervalley scattering triggered by point defects, which opens an additional Dyakonov–Perel-like relaxation channel for in-plane spins.

Due to the fast experimental progress in the field, the theory is generally lagging but there are notable exceptions. A microscopic theory of spin dynamics for graphene-based van der Waals heterostructures with $C_{3v}$ point-group symmetry was put forward in [35]. Moreover, a controlled diagrammatic approach to calculating linear response functions in the presence of disorder and generic proximity effects was developed in a recent series of works [26, 36–39]. An electrical detection scheme that enables full disentanglement of competing SOC transport effects in diffusive lateral spin-valve devices was also proposed recently in [40]. These early works highlighted the key role played by symmetry, quantum geometry and impurity scattering in the spin dynamics and spin–orbit-coupled transport phenomena, such as the spin Hall effect (SHE) [41], in honeycomb layers. The diagrammatic approach has proven ideal for the study of the weak-disorder limit relevant for clean samples with large mean free paths, where numerical simulations have traditionally struggled [42, 43]. Interestingly, the emergence of noncoplanar **k**-space spin textures in broken inversion symmetry conditions was shown to allow for a robust skew-scattering-induced SHE that dominates over the intrinsic (spin-Berry-curvature) contribution in the clean limit, while not requiring spin-dependent disorder potentials [36]. On the other hand, tight-binding methods have provided useful insights into the highly disordered limit (e.g. via simulations of extrinsic SHE efficiency in samples with a high coverage of adatoms [44]). However, a unified semiclassical description of spin–orbit-coupled transport effects in the presence of generic time- and space-dependent perturbations is still lacking, even for the simplest case of $C_{6v}$-symmetric graphene heterostructures. The aim of this paper is to fill this gap by developing a theoretical framework that encompasses all the known phenomenology and has the potential to provide new predictions for the numerous opto-spintronic phenomena supported by van der Waals materials [40, 42, 45–48]. To that end, we devise a Green's function *inverse diffuson* approach that respects the SO(5) algebraic structure of spin–orbit-coupled 2D Dirac fermions (rather than projecting out the sublattice degree of freedom to obtain a simplified description in terms of Bloch-type equations [49]), which can be used to derive quantum kinetic equations in a simple and mathematically transparent fashion. This extension of the powerful *diffuson* approach originally developed for 2D electron gases [50, 51] will allow us not only to keep track of the entangled dynamics of pseudospin and spin observables, but also to obtain useful analytical expressions for linear response functions to generalized fields of experimental relevance, such as Zeeman-type spin-injection fields.

This paper is organized as follows. In section 1.1, we introduce the 2D Dirac–Rashba model capturing the low-energy dynamics of $C_{6v}$-symmetric graphene heterostructures. Section 1.2 describes the diagrammatic framework and the semiclassical approximation used in treating scattering effects. In section 2 we derive the semiclassical drift–diffusion transport equations for the experimentally accessible macroscopic observables and discuss various features and applications of the formalism. Section 3 presents our conclusions.

### 1.1. The 2D Dirac–Rashba model

For our theoretical study of spin–charge-coupled transport in spin–orbit-coupled graphene, we use a model of noninteracting electrons subject to a random impurity potential. Because we are interested in emergent phenomena stemming from interfacial breaking of inversion symmetry, we assume that the BR interaction is the dominant SOC effect (see figures 1(a) and (b)) [25, 52]. The effective Hamiltonian at the $K$ valley can be written in terms of tensor products of Pauli matrices $\sigma_a \otimes s_b$ $(a, b = x, y, z)$ acting on the pseudospin–spin space as [53]

$$H = \int d^2\mathbf{x}\, \Psi^\dagger(\mathbf{x}) \left[ v\sigma_\mu \left( p^\mu + \mathcal{A}^\mu \right) + V(\mathbf{x}) \right] \Psi(\mathbf{x}), \tag{1}$$

where $v \simeq 10^6$ m s$^{-1}$ is the bare Fermi velocity of the massless Dirac fermions, $p^\mu = (-\varepsilon/v, -\imath\hbar\nabla)$ is the energy–momentum 3-vector, $\mathcal{A}^\mu = \sum_{a=x,y,z} \mathcal{A}^\mu_a s_a$ $(\mu = 0, x, y, z)$ is the non-Abelian SU(2) gauge field capturing all spin-dependent effects and $V(\mathbf{x})$ is the impurity potential. Here, summation over repeated indices is implied with $\sigma_0$ denoting the identity matrix. The BR effect with coupling strength $\lambda$ is encoded in the gauge field components $\mathcal{A}^x_y = -\mathcal{A}^y_x = \lambda/v$, which generate the corresponding spin–orbit interaction via minimal coupling $[\mathcal{H}_{\mathrm{BR}} = \lambda(\boldsymbol{\sigma} \times \boldsymbol{s})_z]$. Equation (1) has been dubbed the 2D Dirac–Rashba model in recent literature [26, 36]. We are not concerned with purely extrinsic transport phenomena induced by spin–orbit-active impurities (i.e. random SOC), which have been the object of detailed microscopic analysis in early work [13, 54–58]. Rather, our focus here is on the transport properties of spin–helical 2D Dirac fermions realized in graphene-based heterostructures with a dilute concentration of spin-transparent impurities and a well-established (i.e. spatially uniform) BR effect.

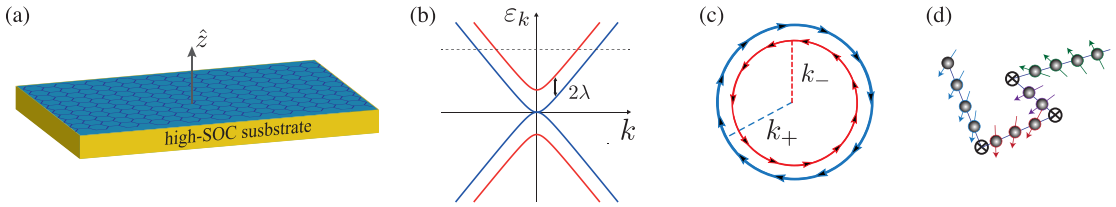


**Figure 1.** (a) Graphene placed on a substrate. The breaking of mirror reflection symmetry $z \to -z$ is responsible for the emergence of a BR effect. (b) Energy dispersion near a $K$ point. The BR coupling lifts the spin degeneracy and opens a spin gap. Blue (red) curves correspond to spin majority (minority) bands. (c) Tangential winding of the spin texture outside the spin gap ($|\varepsilon| > 2|\lambda|$). (d) Dyakonov–Perel spin-relaxation mechanism is operative in samples with a weak BR effect ($|\lambda| \ll \eta$, with $\eta$ the quasiparticle broadening). Crosses indicate scattering centers and colored arrows the spin vector.

The dispersion relation of the minimal Dirac–Rashba model, $\mathcal{H}_{0\mathbf{k}} = \hbar v \boldsymbol{\sigma} \cdot \mathbf{k} + \mathcal{H}_{\mathrm{BR}}$, reads as

$$\varepsilon_{\mu\nu}(\mathbf{k}) = \mu\lambda + \nu\sqrt{\lambda^2 + \hbar^2 v^2 k^2}\,, \tag{2}$$

where $\mu(\nu) = \pm 1$ label, respectively, the spin-helicity and polarity of charge carriers (figure 1(b)). The BR effect lifts the spin degeneracy and locks the spin polarization and wavevector at right angles, leading to a spin-helical configuration in $\mathbf{k}$-space (figure 1(c)). The Dirac nature of the carriers enables a low electronic density regime characterized by a simply-connected Fermi surface with well defined spin-helicity (i.e. $\mu = -1$), akin to the surface states of topological insulators, with interesting consequences for spin-charge conversion effects [35].

The equilibrium spin polarization associated with the Bloch eigenstates of $\mathcal{H}_{0\mathbf{k}}$ is easily computed as

$$\langle \mathbf{S} \rangle_{\mu\nu\mathbf{k}} = \frac{\hbar}{2}\langle \boldsymbol{s} \rangle_{\mu\nu\mathbf{k}} = -\frac{\hbar}{2}\mu \langle \boldsymbol{\sigma} \rangle_{\mu\nu\mathbf{k}} \times \hat{\mathbf{z}}\,, \tag{3}$$

where $\langle \boldsymbol{\sigma} \rangle_{\mu\nu\mathbf{k}} = (1/\hbar v)\nabla_{\mathbf{k}}\epsilon_{\mu\nu}(\mathbf{k})$ is the expectation value of the pseudospin polarization vector. The spin winding of the Fermi surface is shared with other surfaces possessing broken inversion symmetry, but unlike conventional spin-helical states, its energy dependence reflects a spin-angular momentum transfer between spin and pseudospin channels. Such a spin-pseudospin coupling is responsible for the conspicuous wavevector dependence of the equilibrium spin texture (equation (3)). Indeed, the spin-polarization magnitude is vanishing at the corners of the first Brillouin zone, where the band velocity is vanishing ($\langle \boldsymbol{\sigma} \rangle_{\mu\nu\mathbf{k}\to 0} = 0$). Away from the zone corners $K$ and $K'$, the spin texture magnitude increases monotonically with the Fermi wavevector until it saturates away from the spin gap (i.e. for $|\varepsilon| \gtrsim 2|\lambda|$). As noted by Rashba [25], the strong momentum-dependence of the spin texture at low energies is a unique fingerprint of BR-coupled 2D Dirac fermions.

The random potential in equation (1), which in this work is assumed to be scalar, affects the spin dynamics of charge carriers by inducing scattering between electronic states with different effective Larmor fields $\boldsymbol{\Omega}_{\mu\nu\mathbf{k}} = \lambda\langle \mathbf{s} \rangle_{\mu\nu\mathbf{k}} \approx -\mu\nu\lambda\hat{\mathbf{k}} \times \hat{z}$ for $|\varepsilon| \gg |\lambda|$. Due to the random change of precession axis, an initial nonequilibrium spin polarization will decay exponentially with time. In the standard weak-SOC regime (realized in systems with a small spin splitting compared to the disorder-induced broadening [59–61]), the spin-relaxation rate is $\tau_s^{-1} \propto \lambda^2\tau$, where $\tau$ is the elastic scattering time (figure 1(d)). Interestingly, the spin-relaxation rate of out-of-plane spins (i.e. polarized along the $\hat{z}$-axis) is twice that of in-plane spins ($\tau_{s,\perp}/\tau_{s,\parallel} = 1/2$), which could provide an experimentally detectable signature of BR effect using Hanle-type spin precession measurements [62, 63]. Impurity scattering also plays a key role in coupled spin–charge transport phenomena, profoundly affecting the efficiency of spin Hall and spin-charge conversion (spin-galvanic) effects, even in the clean limit with $|\varepsilon|\tau \gg 1$, as we shall see below.

### 1.2. Theoretical framework

To derive a rigorous microscopic picture of coupled spin-charge transport, we evaluate the density matrix response function employing many-body perturbation theory methods [64–66]. Our aim is to generalize the familiar *diffuson* approach for 2D electron gases [50, 51] to accommodate the enlarged SO(5) Clifford algebra of 2D Dirac fermions. Because we are interested in the diffusive regime realized in weakly disordered samples with $|\varepsilon|\tau \gg 1$, we neglect quantum corrections arising from weak localization and higher-order spin-orbit scattering effects, such as quantum side jumps and diffractive skew scattering [57, 58, 67]. In the diagrammatic language, such semiclassical approximation amounts to discarding crossing diagrams encoding coherent multiple impurity scattering events, as well as higher-order noncrossing diagrams with a

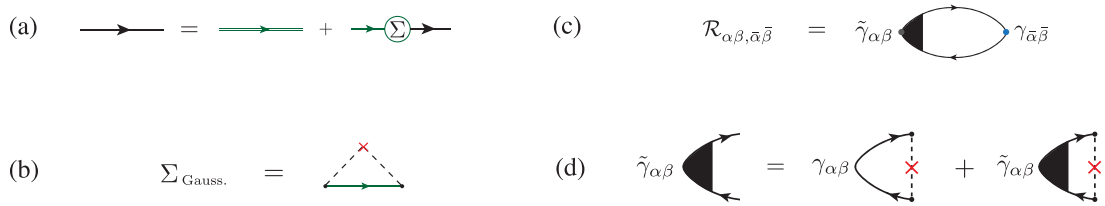


**Figure 2.** (a)–(d) Diagrammatic scheme for the evaluation of the linear response density matrix. Green (black) solid line with an arrow denotes the free (disorder-averaged) Green's function. Dashed lines depict scattering potential insertions ($u_0$) and the cross represents the impurity density ($n_i$).

perturbation parameter $1/(|\varepsilon|\tau) \ll 1$ [57]. Unless stated otherwise, we work in natural units with $\hbar \equiv 1 \equiv e$. Additionaly, for ease of notation, we assume throughout that $\varepsilon, \lambda > 0$.

The central object in our approach is the real-time retarded(R)/advanced(A) single-particle Green's function ($a = A, R \equiv -, +$) defined as

$$G^a(\mathbf{x}, \mathbf{x}'; t - t') = \mp \imath \left\langle 0 | T \left[ \Psi(\mathbf{x}, t), \Psi^\dagger(\mathbf{x}', t') \right] | 0 \right\rangle \theta(\pm t \mp t'), \tag{4}$$

where $\Psi^\dagger(\mathbf{x}, t)$ [$\Psi(\mathbf{x}, t)$] are 4-component field operators creating (annihilating) a 2D Dirac fermion at position $\mathbf{x}$ and time $t$, $T$ is the time-ordering symbol and $\theta(.)$ is the Heaviside step function. After disorder averaging (indicated below by an overline), the Green's function in momentum-frequency space acquires the familiar form

$$\mathcal{G}^a_{\mathbf{k}}(\varepsilon) = \frac{1}{[\mathcal{G}^a_{0\mathbf{k}}(\varepsilon)]^{-1} - \Sigma^a_{\mathbf{k}}(\varepsilon)}, \tag{5}$$

where $\mathcal{G}^a_{0\mathbf{k}}(\varepsilon) = [\varepsilon - v\boldsymbol{\sigma} \cdot \mathbf{k} - \lambda\, (\boldsymbol{\sigma} \times \mathbf{s}) \cdot \hat{z} + \imath a 0^+]^{-1}$ is the Fourier transform of the clean Green's function and

$$\Sigma^a_{\mathbf{k}}(\varepsilon) = \int d(\mathbf{x} - \mathbf{x}')\, e^{-\imath \mathbf{k}(\mathbf{x} - \mathbf{x}')} \overline{\langle \mathbf{x}' | V \frac{1}{1 - G^a_0(\varepsilon) V} | \mathbf{x} \rangle} \tag{6}$$

is the quasiparticle self energy in the noncrossing approximation. For uncorrelated short-range impurity potentials, the self energy is $\mathbf{k}$-independent, and so we set $\Sigma^a_{\mathbf{k}}(\varepsilon) \equiv \Sigma^a(\varepsilon)$ from here onwards.

In order to keep our discussion as simple as possible, we compute the self energy under the assumption of weak Gaussian disorder. This will simplify our analytical treatment significantly while capturing the essential physics [68]. Diagrammatically, the weak disorder approximation amounts to retaining only the contribution from the 'rainbow' diagram with two impurity potential lines; see figures 2(a) and (b). Replacing the explicit form of the two-point correlator $\overline{V(\mathbf{x}) V(\mathbf{x}')} = n_i u_0^2 \delta(\mathbf{x} - \mathbf{x}')$ in the Dyson expansion of the self energy, where $n_i$ is the impurity areal density and $u_0$ is the potential strength, one arrives at

$$\Sigma^{\pm}(\varepsilon) = \mp\, (\imath/2\tau) \left[ \theta(\varepsilon - 2\lambda) + \theta(2\lambda - \varepsilon) \left( 1 + \sigma_z s_z - \frac{\varepsilon}{\lambda} \gamma_r \right) \frac{\lambda}{\varepsilon} \right], \tag{7}$$

where $1/2\tau \equiv \eta = n_i u_0^2 \varepsilon / 4v^2$ is the quasiparticle broadening and $\gamma_r \equiv (\sigma_x s_y - \sigma_y s_x)/2$. The existence of two distinct transport regimes at low energies (i.e. $\varepsilon > 2\lambda$ and $\varepsilon < 2\lambda$) is a unique feature of the 2D Dirac–Rashba model, which is responsible for the existence of a maximum in current-induced spin polarization efficiency when the (gate-tunable) Fermi energy lies precisely at the spin-gap edge [26].

In this paper, we are primarily interested in the diffusive coupled spin–charge dynamics which occur in graphene flakes with weak proximity-induced SOC at moderate–high charge carrier densities ($\varepsilon\tau \gg 1 \gg \lambda\tau$) [37]. The condition $\varepsilon \gg \lambda$ implies that the BR-slit bands with opposite spin helicities are occupied at the Fermi level. To study the behavior of the system away from equilibrium, it is convenient to introduce the generalized one-particle density operator

$$\hat{\rho}_{\alpha\beta}(\mathbf{x}; t) = \Psi^\dagger(\mathbf{x}, t)\, \gamma_{\alpha\beta}\, \Psi(\mathbf{x}, t), \tag{8}$$

where $\gamma_{\alpha\beta} = \sigma_\alpha \otimes s_\beta$ (with $\alpha, \beta = 0, x, y, z$) span the vector space of Hermitian $4 \times 4$ matrices. The density matrix characterizing a given nonequilibrium state can be expanded as a linear combination of the Clifford algebra basis elements, such that

$$\rho(\mathbf{x}, t) = \frac{1}{d} \sum_{\alpha,\beta = 0,x,y,z} \gamma_{\alpha\beta} \left\langle \hat{\rho}_{\alpha\beta}(\mathbf{x}, t) \right\rangle, \tag{9}$$

where $\langle\ldots\rangle$ denotes quantum and disorder averages and $d = \dim H \equiv 4$ is a normalization factor. The expectation value of a generic local observable, $\mathcal{O} = \sum_{\alpha\beta} \mathcal{O}_{\alpha\beta}\gamma_{\alpha\beta}$, is obtained according to

$$\langle \mathcal{O}(\mathbf{x},t)\rangle := \mathrm{tr}\,[\mathcal{O}\,\rho(\mathbf{x},t)] = \sum_{\alpha,\beta} \mathcal{O}_{\alpha\beta}\,\rho_{\alpha\beta}(\mathbf{x},t)\,, \tag{10}$$

where tr indicates the trace over internal degrees of freedom and $\rho_{\alpha\beta}(\mathbf{x},t) \equiv \langle\hat{\rho}_{\alpha\beta}(\mathbf{x},t)\rangle$.

In this work we are concerned with the semiclassical dynamics of typical spin transport observables, such as the spin-polarization density and the spin current density. Thus, it is more convenient to work directly with the deviation from equilibrium of the expectation values, i.e. $\langle\delta\mathcal{O}(\mathbf{x},t)\rangle := \mathrm{tr}\,[\mathcal{O}\,\delta\rho(\mathbf{x},t)]$ with $\delta\rho_{\alpha\beta}(\mathbf{x},t) := \rho_{\alpha\beta}(\mathbf{x},t) - \rho^0_{\alpha\beta}$. Here, $\rho^0_{\alpha\beta}$ denotes the equilibrium part of the (disorder-averaged) density matrix. The macroscopic observables of interest to us are the charge density, $N$, spin polarization density, $S^a$ $(a = x,y,z)$, charge current density, $J_i$ $(i = x,y)$, and spin current density, $\mathcal{J}^a_i$. The corresponding expectation values away from equilibrium are defined as

$$\{\delta N, \delta S^a, \delta J_i, \delta\mathcal{J}^a_i\} = \{-e\delta\rho_{00},\, \frac{\hbar}{2}\delta\rho_{0a},\, -ev\delta\rho_{i0},\, \frac{\hbar v}{2}\delta\rho_{ia}\}\,, \tag{11}$$

where we have temporarily reinstated $\hbar$ and $e$ to distinguish between charge and spin currents.

The interaction Hamiltonian is $V(t) = \int d^2\mathbf{x}\,\Psi^\dagger(\mathbf{x})\,[\mathcal{H}_{\mathrm{int}}(\mathbf{x},t)]\,\Psi(\mathbf{x})$ with

$$\mathcal{H}_{\mathrm{int}}(\mathbf{x},t) = v\sum_{\alpha,\beta}\gamma_{\alpha\beta}\,\mathcal{A}^{\mathrm{ext}}_{\alpha\beta}(\mathbf{x},t)\,, \tag{12}$$

where $\mathcal{A}^{\mathrm{ext}}_{\alpha\beta}(\mathbf{x},t)$ $(\alpha,\beta = 0,x,y,z)$ spans the Clifford algebra and thus describes any type of charge–spin perturbation applied to the system. In section 2.1, we shall show that the linear response density matrix $\delta\rho(\mathbf{x},t)$, when properly coarse-grained over typical length and time scales (i.e. $|\mathbf{x}| \gg l \equiv v\tau$ and $t \gg \tau$), is governed by an enlarged $16\times 16$ *diffuson Hamiltonian* that is the SO(5) analogue of the familiar inverse density fluctuation propagator of 2D electron gases [50, 51, 69] and topological insulators [70, 71]. In section 2.2, the linear response machinery will be applied to derive the full set of drift–diffusion transport equations for the variables $\delta N$, $\delta S^a$, $\delta J_i$ and $\delta\mathcal{J}^a_i$, and thus establish a rigorous microscopic picture for the coarse-grained dynamics of the problem. In the following, we define $N \equiv \delta N$, $S^a \equiv \delta S^a$, $J_i \equiv \delta J_i$ and $\mathcal{J}^a_i \equiv \delta\mathcal{J}^a_i$ for ease of notation.

## 2. Results

### 2.1. Diffuson Dirac Hamiltonian

We start by setting up the formalism needed to derive a quantum kinetic equation for BR-coupled 2D Dirac fermions. From standard linear response theory, the zero temperature density matrix is given by

$$\delta\rho_{\alpha\beta}(\mathbf{x},t) = \sum_{\bar\alpha,\bar\beta=0,x,y,z}\int d\mathbf{x}'\int dt'\,\mathcal{R}_{\alpha\beta,\bar\alpha\bar\beta}(\mathbf{x}-\mathbf{x}',t-t')\,v\mathcal{A}^{\mathrm{ext}}_{\bar\alpha\bar\beta}(\mathbf{x}',t')\,, \tag{13}$$

where

$$\mathcal{R}_{\alpha\beta,\bar\alpha\bar\beta}(\mathbf{x}-\mathbf{x}',t-t') = -\imath\theta(t-t')\langle\overline{[\hat{\rho}_{\alpha\beta}(\mathbf{x},t),\hat{\rho}_{\bar\alpha\bar\beta}(\mathbf{x}',t')]}\rangle \tag{14}$$

is the retarded response function. Equation (14) is best evaluated in momentum–frequency space using the Green's-function method [66]. A summation of noncrossing two-particle diagrams, as depicted in figures 2(c) and (d), leads to

$$\mathcal{R}_{\alpha\beta,\gamma\delta}(\mathbf{q},\omega) \simeq \frac{\omega}{2\pi i}\sum_{\mathbf{k}}\mathrm{tr}\left\{\gamma_{\alpha\beta}\,\mathcal{G}^R_{\mathbf{k}+\mathbf{q}}(\varepsilon+\omega)\,\tilde\gamma_{\gamma\delta}(\mathbf{q},\omega)\,\mathcal{G}^A_{\mathbf{k}}(\varepsilon)\right\}, \tag{15}$$

where the renormalized vertex operator $\tilde\gamma_{\alpha\beta}(\mathbf{q},\omega)$ satisfies the Bethe–Salpeter equation

$$\tilde\gamma_{\alpha\beta}(\mathbf{q},\omega) = \gamma_{\alpha\beta} + n_i u_0^2\sum_{\mathbf{k}}\mathcal{G}^R_{\mathbf{k}+\mathbf{q}}(\varepsilon+\omega)\,\tilde\gamma_{\alpha\beta}(\mathbf{q},\omega)\,\mathcal{G}^A_{\mathbf{k}}(\varepsilon)\,. \tag{16}$$

Next, we project both sides of equation (16) onto the Dirac matrices and define

$$\tilde{\boldsymbol{\gamma}}_{\alpha\beta}(\mathbf{q},\omega) = (\tilde\gamma_{\alpha\beta 00}(\mathbf{q},\omega),\ldots,\tilde\gamma_{\alpha\beta zz}(\mathbf{q},\omega))^T, \tag{17}$$

**Table 1.** Classification of Dirac matrices and corresponding observables under $C_2$-rotation, mirror-reflection $R_x$ and time-reversal operation. Sublattice-staggered densities are indicated with subscript '$s$'.

| | $\gamma_{00}$ | $\gamma_{01}$ | $\gamma_{02}$ | $\gamma_{03}$ | $\gamma_{10}$ | $\gamma_{11}$ | $\gamma_{12}$ | $\gamma_{13}$ | $\gamma_{20}$ | $\gamma_{21}$ | $\gamma_{22}$ | $\gamma_{23}$ | $\gamma_{30}$ | $\gamma_{31}$ | $\gamma_{32}$ | $\gamma_{33}$ |
|---|---|---|---|---|---|---|---|---|---|---|---|---|---|---|---|---|
| $\mathcal{O}$ | $N$ | $S^x$ | $S^y$ | $S^z$ | $J_x$ | $\mathcal{J}_x^x$ | $\mathcal{J}_x^y$ | $\mathcal{J}_x^z$ | $J_y$ | $\mathcal{J}_y^x$ | $\mathcal{J}_y^y$ | $\mathcal{J}_y^z$ | $N_s$ | $S_s^x$ | $S_s^y$ | $S_s^z$ |
| $C_2$ | $+1$ | $-1$ | $-1$ | $+1$ | $-1$ | $+1$ | $+1$ | $-1$ | $-1$ | $+1$ | $+1$ | $-1$ | $+1$ | $-1$ | $-1$ | $+1$ |
| $R_x$ | $+1$ | $-1$ | $+1$ | $-1$ | $+1$ | $-1$ | $+1$ | $-1$ | $-1$ | $+1$ | $-1$ | $+1$ | $-1$ | $+1$ | $-1$ | $+1$ |
| $\mathcal{T}$ | $+1$ | $-1$ | $-1$ | $-1$ | $-1$ | $+1$ | $+1$ | $+1$ | $-1$ | $+1$ | $+1$ | $+1$ | $-1$ | $+1$ | $+1$ | $+1$ |

with $\tilde{\gamma}_{\alpha\beta\varrho\varsigma}(\mathbf{q},\omega) = (1/d)\,\mathrm{tr}[\gamma_{\varrho\varsigma}\,\tilde{\gamma}_{\alpha\beta}(\mathbf{q},\omega)]$, to obtain the renormalized vertex in a suitable closed form

$$\tilde{\gamma}_{\alpha\beta}(\mathbf{q},\omega) = (I - [M(\mathbf{q},\omega)]^T)^{-1}\gamma_{\alpha\beta}\,, \tag{18}$$

where $\gamma_{\alpha\beta} = (0,\ldots,1,\ldots,0)^T$ is an auxiliary vector with nonzero component $(\gamma_{\alpha\beta})_{\alpha\beta} = 1$, $I$ is the identity matrix, $T$ denotes the transpose operation and $M$ is a square matrix of 'bubbles' with elements

$$M_{\mu\nu,\varrho\varsigma}(\mathbf{q},\omega) = \frac{n_i u_0^2}{d}\sum_{\mathbf{k}}\mathrm{tr}\left[\mathcal{G}^R_{\mathbf{k}+\mathbf{q}}(\varepsilon+\omega)\gamma_{\mu\nu}\mathcal{G}^A_{\mathbf{k}}(\varepsilon)\gamma_{\varrho\varsigma}\right]. \tag{19}$$

We may now recast the Fourier space response function into a more compact form $\mathcal{R}_{\alpha\beta,\bar{\alpha}\bar{\beta}}(\mathbf{q},\omega) = -\imath\omega\nu_0\mathcal{D}_{\alpha\beta,\bar{\alpha}\bar{\beta}}(\mathbf{q},\omega)$, where $\nu_0 = \varepsilon/\pi v^2$ is the density of states per spin and

$$\mathcal{D}_{\alpha\beta,\bar{\alpha}\bar{\beta}}(\mathbf{q},\omega) = \tau\left(\tilde{\gamma}_{\bar{\alpha}\bar{\beta}\alpha\beta}(\mathbf{q},\omega) - \delta_{\alpha\bar{\alpha}}\delta_{\beta\bar{\beta}}\right) \tag{20}$$

is the so-called *diffuson* (here, $\delta_{\alpha\beta}$ is the Kronecker delta symbol). Its inverse, the *diffuson Hamiltonian* $\mathcal{H}_{\mathcal{D}} \equiv \mathcal{D}^{-1}$,

$$\mathcal{H}_{\mathcal{D}}(\mathbf{q},\omega) = \frac{1}{\tau}\left(\left(I - [M(\mathbf{q},\omega)]^T\right)^{-1} - I\right)^{-1}, \tag{21}$$

provides the kernel of the linear response quantum kinetic equation

$$\mathcal{H}_{\mathcal{D}}(\mathbf{q},\omega)\cdot\delta\vec{\rho}(\mathbf{q},\omega) = -\imath v\omega\nu_0\vec{\mathcal{A}}_{\mathrm{ext}}(\mathbf{q},\omega)\,, \tag{22}$$

where $\delta\vec{\rho}(\mathbf{q},\omega) \equiv (\delta\rho_{00}(\mathbf{q},\omega),\ldots,,\delta\rho_{zz}(\mathbf{q},\omega))^T$ and $\vec{\mathcal{A}}_{\mathrm{ext}}(\mathbf{q},\omega) \equiv (\mathcal{A}^{\mathrm{ext}}_{00}(\mathbf{q},\omega),\ldots,A^{\mathrm{ext}}_{zz}(\mathbf{q},\omega))^T$ are the Fourier-space components of the one-particle density matrix and generalized external vector potential, respectively.

Let us briefly discuss the general structure of $\mathcal{H}_{\mathcal{D}}(\mathbf{q},\omega)$ in the long wavelength limit of interest to us. Zero entries in the $16\times16$ bubble matrix $M(0,\omega)$ can be readily identified by applying the following $C_{6v}$ point-group operations [72]: (i) $C_2$ rotation exchanging sublattices and (ii) mirror-reflection $R_x$ leaving sublattices invariant. For example, the bubbles $M_{00,0a}(0,\omega)$, encoding charge-density–spin-density-type responses ($a = x,y,z$), vanish identically because the associated vertices ('00' and '0$a$') transform differently under at least one unitary symmetry. Overall, there are 64 non-zero bubbles in the long-wavelength $\mathbf{q}\to0$ limit. The symmetry classification is summarized in table 1.

We now turn to the spin–charge eigenmodes sustained by the system. The first step is to compute the gradient expansion of equation (21). Working in the diffusive regime ($\epsilon\tau \gg 1 \gg \lambda\tau$) greatly simplifies matters due to many bubbles being parametrically small. To leading order in $v|\mathbf{q}|$ and $\omega\tau$, we find

$$\mathcal{H}_{\mathcal{D}}(\mathbf{q},\omega) \simeq \imath\omega Q - \imath\mathbf{P}\cdot\mathbf{q} + L\,, \tag{23}$$

where $Q$, $P_i$ and $L$ are $16\times16$ matrices given by $Q = -\imath(\nabla_\omega\mathcal{H}_{\mathcal{D}}(0,\omega))_{\omega=0}$, $\mathbf{P} = \imath(\partial_{\mathbf{q}}\mathcal{H}_{\mathcal{D}}(\mathbf{q},0))_{\mathbf{q}=0}$ and $L = \mathcal{H}_{\mathcal{D}}(0,0)$. The calculation of these matrices is rather cumbersome, yielding unwieldy expressions for the matrices $Q = Q(\varepsilon,\lambda,\tau)$, $P_i = P_i(\varepsilon,\lambda,\tau)$ and $L = L(\varepsilon,\lambda,\tau)$. We therefore provide the explicit form of the equation (23) in the appendix, from which $Q$, $P_i$ and $L$ can be inferred.

The *diffuson* Hamiltonian in equation (23) is linear in the wavevector $\mathbf{q}$ due to the Dirac nature of the low-lying excitations in graphene heterostructures. The *diffuson* spectrum at low energies is shown in figure 3. The quadratic dispersion of the gapless mode follows from the diffusive pole structure of the density–density response, i.e. $[\mathcal{R}_{00,00}(\mathbf{q},0)]^{-1} \sim (v\tau|\mathbf{q}|)^2$. For $\mathbf{q}\neq0$, this mode is an admixture of charge $N$, spin current $\mathcal{J}_i^a$ and spin polarization $S^{x,y}$ fluctuations. The gapped states, on the other hand, describe eigenmodes of the nonequilibrium spin polarization $S^a$ [73]. Note that two of these states ($S^{x,y}$) are degenerate at $\mathbf{q}=0$ due to the rotational ($C_{v\infty}$) symmetry of the single-particle Hamiltonian (equation (1)). Their gaps at $\mathbf{q}=0$ are given by $\Delta_s \equiv \Delta_\parallel \simeq (\lambda/\eta)^2$ for the $S^{x,y}$- and $\Delta_\perp \simeq 2\Delta_\parallel$ for the $S^z$-mode. The twice

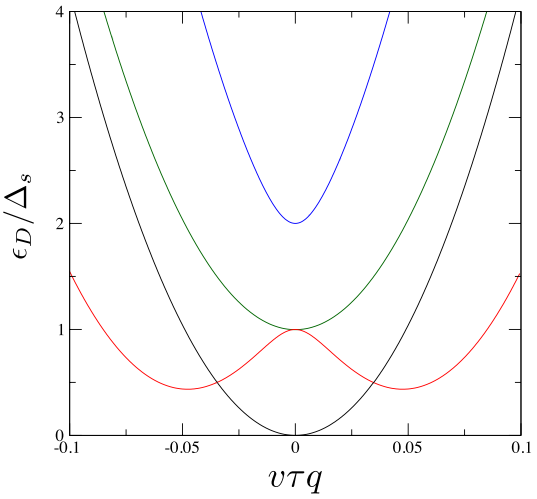


**Figure 3.** Spectrum of the *diffuson* Hamiltonian in units of spin gap $\Delta_s$. Only low-lying states are shown. Parameters: $\varepsilon = 0.3$ eV, $\lambda = 0.1$ meV and $\eta = 1/2\tau = 2$ meV. The curves are obtained numerically from $\epsilon_D(q) = \mathrm{Re}\,\lambda(q,0)$ with $q = |\mathbf{q}|$, where $\lambda(q,\omega)$ are the complex eigenvalues of the *diffuson* Hamiltonian matrix (equation (21)).

as fast dephasing of out-of-plane spin fluctuations is a fingerprint of BR SOC, a feature which is known to survive even in the strong (unitary) scattering regime [37].

The low-lying modes shown in figure 3 are remarkably similar to those of a BR-coupled 2D electron gas [51]. We verified that the *diffuson* spectra of the two Rashba models can be exactly mapped onto each other, despite their distinctly different *diffuson* Hamiltonians (i.e. $4\times 4$ Schrödinger-like for 2D electron gases and $16\times 16$ Dirac-like for graphene). Defining $\xi = 2v|\mathbf{q}|\tau$, the eigenvalues of $\mathcal{H}_{\mathcal{D}}(\mathbf{q},0)$ in the limit $v|\mathbf{q}| \ll 1$ are given by $\epsilon_D^0 = \xi^2$, $\epsilon_D^1 = \xi^2 + \Delta_s$ and $\epsilon_D^{\pm} = \xi^2 + \Delta_s\left(\frac{3}{2} \pm \frac{1}{2}\sqrt{1 + 16\xi^2/\Delta_s}\right)$. The Rashba *diffuson* eigenvalues derived by Wenk *et al* [51] are recovered by letting $\lambda/v \to 2m_e\alpha_2$, where $m_e$ is the effective electron mass and $\alpha_2$ the Rashba parameter. The existence of such a mapping reflects the same basic spin-relaxation (Dyakonov–Perel) mechanism at work. Indeed, our findings put on a firm ground previous heuristic arguments [36, 37] for the equivalence of two models in the weak SOC regime. The remaining $16 - 4 = 12$ modes in the Dirac–Rashba model are characterized by very large gaps ($\Delta_s^+ \gtrsim 1/2 \gg \Delta_s$), and as such play no role in the diffusive regime.

A comment is in order regarding the validity of our assumptions in the light of recent findings. In the example of figure 3, we considered a small BR coupling of only 0.1 meV, which is in line with density functional theory calculations for clean graphene/group VI dichalcogenide heterostructures [16, 18]. On the other hand, the semi-empirical Slater-Koster parametrization of [74], as well as early magnetotransport measurements [20–24], have found much higher proximity-induced SOC (up to $\approx 10$ meV). Furthermore, a recent joint theory-experiment study suggests that the interfacial Rashba coupling can be made as large as 100 meV, by placing a graphene flake on top of a metallic substrate with a suitable work function mismatch [29]. We note that in any case, the theory developed in this work is expected to remain accurate provided that the Dirac bands remain intact (so that the low-energy picture in figure 1 is justified) and the system is sufficiently disordered so that $\lambda\tau \ll 1$.

### 2.2. Unified coupled spin-charge drift-diffusion equations

The quantum kinetic equation governing the one-particle reduced density matrix in the large distance and long time limits is obtained after an inverse Fourier transform ($-\imath\omega \to \partial_t$ and $\imath q_i \to \nabla_i$) of equation (23) as

$$\mathcal{H}_{\mathcal{D}}\cdot\delta\vec{\rho}(\mathbf{x},t) = \left(-Q\frac{\partial}{\partial t} - \sum_{i=x,y} P_i\nabla_i + L\right)\cdot\delta\vec{\rho}(\mathbf{x},t) = \nu\nu_0\partial_t\vec{\mathcal{A}}_{\mathrm{ext}}(\mathbf{x},t)\,. \tag{24}$$

Transport equations for the coarse-grained variables $N(\mathbf{x},t) = -\delta\rho_{00}(\mathbf{x},t)$, $S^a(\mathbf{x},t) = \frac{1}{2}\delta\rho_{0a}(\mathbf{x},t)$, $J_i(\mathbf{x},t) = -v\delta\rho_{i0}(\mathbf{x},t)$ and $\mathcal{J}_i^a(\mathbf{x},t) = \frac{v}{2}\delta\rho_{ia}(\mathbf{x},t)$ can now be derived by replacing the $16\times 16$ matrices $Q = Q(\varepsilon,\lambda,\tau)$, $P_i = P_i(\varepsilon,\lambda,\tau)$ and $L = L(\varepsilon,\lambda,\tau)$ with their explicit forms (see appendix). To leading order in $1/\varepsilon\tau$ and $\lambda\tau$, we obtain

$$\partial_t N + \nabla\cdot J = 0\,, \tag{25}$$

**Table 2.** Coefficients in the coupled spin–charge drift–diffusion equations. Only nonzero components are listed.

| | | |
|---|---|---|
| $\Lambda$ | Spin density precession | $\Lambda^{zx}_{x} = \Lambda^{zy}_{y} = -1,\ \Lambda^{xx}_{z} = \Lambda^{yy}_{z} = 1$ |
| $\Gamma$ | Spin current transfer | $\Gamma^{xx}_{xz} = \Gamma^{yy}_{yz} = 1,\ \Gamma^{zx}_{xx} = \Gamma^{zy}_{xy} = \Gamma^{zx}_{yx} = \Gamma^{zy}_{yy} = -1, \Gamma^{yy}_{xz} = \Gamma^{xx}_{yz} = 1$ |
| $\Omega$ | Spin current precession | $\Omega^{x}_{xz} = \Omega^{y}_{yz} = 1,\ \Omega^{z}_{xx} = \Omega^{z}_{yy} = -1$ |
| $\Upsilon$ | Spin current swapping | $\Upsilon^{xy}_{xy} = \Upsilon^{yx}_{yx} = 1,\ \Upsilon^{yy}_{xx} = \Upsilon^{xx}_{yy} = -1$ |

$$\partial_t S^a + \nabla\cdot\mathcal{J}^a = \frac{2\lambda}{v}\Lambda^{ab}_{c}\mathcal{J}^c_b + \frac{\nu_0}{2}\mathcal{B}^a\,, \tag{26}$$

$$\partial_t J_i + \frac{v^2}{2}\nabla_i N = -\frac{J_i}{2\tau} - \frac{4\lambda^2}{\epsilon}\epsilon_{ij}\mathcal{J}^z_j + \frac{\nu_0}{2}v^2 E_i\,, \tag{27}$$

$$\partial_t \mathcal{J}^a_i + \frac{v^2}{2}\nabla_i S^a + v\lambda\tau\Gamma^{ab}_{ic}\nabla_b\mathcal{J}^c_i = -\frac{\mathcal{J}^a_i}{2\tau} + v\lambda\Omega^a_{ic}S^c + \lambda^2\tau\Upsilon^{ab}_{ic}\mathcal{J}^c_b - \delta_{az}\epsilon_{ij}\frac{\lambda^2}{\varepsilon}J_j\,, \tag{28}$$

where $E_i = -\partial_t\mathcal{A}^{\rm ext}_{i0}$ is the externally applied electric field and $\mathcal{B}^a = (1/v)\,\partial_t\mathcal{A}^{\rm ext}_{0a}(\mathbf{x},t)$ is the external Zeeman field ('spin injection field') that induces a nonequilibrium spin density [75]. The coefficients $\Lambda^{ab}_c, \Gamma^{ab}_{ic}, \Omega^a_{ic}$ and $\Upsilon^{ab}_{ic}$ are listed in table 2 and $\varepsilon_{ij}$ denotes the rank-2 Levi-Civita symbol ($i,j = x,y$). Different perturbations (e.g. a spin-dependent electric field $\mathcal{E}^a_i = -\partial_t\mathcal{A}_{ia}$) can be easily incorporated via a suitable parameterization of the generalized external vector potential entering equation (24).

The drift–diffusion equations (25)–(28) are the main results of this work. Equations (25) and (26) are generalized continuity relations and equations (27) and (28) express the time evolution of the currents as a sum of drift, diffusion, spin precession and spin–charge conversion processes. Standard constitutive relations

$$J_i = -D\nabla_i N - \frac{8\tau\lambda^2}{\varepsilon}\epsilon_{ij}\mathcal{J}^z_j + \nu_0\tau v^2 E_i\,, \tag{29}$$

$$\mathcal{J}^a_i = -D\nabla_i S^a - 2v\lambda\tau^2\Gamma^{ab}_{ic}\nabla_b\mathcal{J}^c_i + 2v\lambda\tau\Omega^a_{ic}S^c + 2\lambda^2\tau^2\Upsilon^{ab}_{ic}\mathcal{J}^c_b - \delta_{a,z}\epsilon_{ij}\frac{2\tau\lambda^2}{\varepsilon}J_j\,, \tag{30}$$

where $D = v^2\tau$ is the diffusion constant [76], hold to good accuracy insofar as $\omega \ll \lambda$. Sublattice-staggered charge $N_{\rm s}$ and spin densities $S^a_{\rm s}$ (see table 1) are conspicuously absent from these relations. In terms of the underlying *diffuson* Hamiltonian, these observables are linked to dispersionless modes with large gaps and are thus effectively decoupled from the low-energy dynamics. We expect such terms to play a role in graphene heterostructures with broken sublattice symmetry [34–36], which is beyond the scope of the this article.

### 2.3. Spin Hall and spin-galvanic effects: the DC regime

Equations (25)–(28) provide a physically transparent scheme to interpret and predict a variety of SOC phenomena of fundamental and technological relevance. Before discussing new applications of the formalism, we briefly revisit two well established results for BR-coupled graphene [26, 36]. We start with the SHE [41], i.e. the appearance of a transverse spin current upon application of a DC charge current, first observed in semiconductors [77, 78]. In graphene with random SOC (e.g. induced by dilute adatoms), a robust SHE can be induced via resonant skew scattering [13, 14, 54–56]. In contrast, for graphene systems with a spatially uniform BR effect, the SHE is strictly vanishing unless supplemented with proximity-induced spin–valley coupling or spin-dependent disorder.

Detailed information on the SHE can be obtained from the drift–diffusion equations with little effort. The so-called *intrinsic* spin Hall angle $\theta^{\rm int}_{\rm sH} = 2\tau\lambda^2/\varepsilon$, which appears explicitly in equations (29)–(30), diverges in the clean limit ($\tau\to\infty$) and does not correspond *per se* to a steady-state transport quantity. The actual spin Hall angle, defined as the ratio between near-equilibrium spin Hall current and applied charge current,

$$\theta_{\rm sH}(\omega) := 2\epsilon_{ij}\left.\frac{\mathcal{J}^z_i}{J_j}\right|_{\mathbf{q}=0,\mathcal{B}^a=0} = \theta^{\rm int}_{\rm sH} + \theta^{\rm dis}_{\rm sH}(\omega)\,, \tag{31}$$

is obtained by solving the system of coupled equations (25)–(28) and receives important disorder corrections even in the clean limit. The 'SHE cancellation' in the DC limit $\theta^{\rm dis}_{\rm sH}(0) = -\theta^{\rm int}_{\rm sH}$ is a fundamental consequence of SU(2)-spin covariance of pure Rashba models as shown by Dimitrova [79]. This result can also be interpreted as the unavoidable outcome for a 2D system with an isotropic and fully in-plane spin texture.

Because the electronic states are admixtures of orthogonal spin states, phase shifts experienced by the spin-up and spin-down components of scattered wavefunctions from scalar impurities cannot be distinguished, implying the absence of skew scattering [36]. As discussed in section 2.4, a robust SHE nevertheless takes place at finite frequencies (i.e. an optical SHE) or when the system is perturbed by a spin-injection field.

Also of interest is the inverse spin-galvanic effect (ISGE), whereby an applied current magnetizes the conduction electrons, thus generating a net spin polarization density [80, 81]. Its microscopic origin lies in the spin–momentum locking of Bloch eigenstates caused by the BR effect (figure 1(c)). While the equilibrium spin polarization averaged over the Fermi surface in a nonmagnetic system must vanish identically (equation (3)), an external electric field effectively breaks the time-reversal symmetry, by causing an imbalance the occupation of states with opposite momenta, which allows the build up of a net transverse spin polarization. The ISGE efficiency can be easily read out from equation (30) by replacing the pure spin current by its steady-state value in the minimal model, i.e. $\mathcal{J}_i^a = 0$. The charge-to-spin conversion efficiency is obtained as:

$$\kappa_{ij} := 2\nu \left.\frac{S^i}{J_j}\right|_{\mathbf{q}=0,\mathcal{B}^a=0} = \epsilon_{ij}\frac{1}{\lambda\tau}\theta_{\rm sH}^{\rm int} = \epsilon_{ij}\frac{2\lambda}{\varepsilon}\,. \tag{32}$$

This relation (first derived in [26]) discloses an optimal spin-charge conversion efficiency at the spin-gap edge, i.e. $\kappa_{xy}(\varepsilon = 2\lambda) = 1$. The ISGE efficiency parameter decays algebraically with the energy of charge carriers, which makes the effect detectable at room temperature over a wide range of charge carrier densities. The robust ISGE in graphene with BR effect has been observed in a recent series of experiments [27–30].

### 2.4. Application: optical spin Hall and spin galvanic effects

As a novel application of the formalism, we derive the optical response of BR-coupled graphene. To this end, we solve the charge–spin drift–diffusion equations (equations (26)–(28)) subject to time-dependent electric and spin-injection fields, with Fourier transforms $E_i(\omega)$ $(i = x, y)$ and $\mathcal{B}_a(\omega)$ $(a = x, y, z)$, respectively. In the Dyakonov–Perel regime with $\omega\tau \ll \lambda\tau \ll 1 \ll \epsilon\tau$, the macroscopic observables of interest are found, after tedious but straightforward calculations, to be

$$J_i(\omega) = \frac{g_v\varepsilon\tau}{\pi}\left[\frac{E_i(\omega)}{1-2\imath\omega\tau} + \epsilon_{ij}\frac{2\lambda}{\nu\varepsilon}\frac{\mathcal{B}_j(\omega)}{\left(1-\imath\omega\tau_{\parallel}\right)\left(1-2\imath\omega\tau\right)}\right], \tag{33}$$

$$S_a(\omega) = \frac{g_v\varepsilon\tau_{s,a}}{2\pi\nu^2}\left[\epsilon_{jaz}\frac{8\nu\lambda^3\tau^2}{\varepsilon}\frac{E_j(\omega)}{\left(1-2\imath\omega\tau\right)\left(1-\imath\omega\tau_{s,a}\right)} + \frac{\mathcal{B}_a(\omega)}{1-\imath\omega\tau_{s,a}}\right], \tag{34}$$

$$\mathcal{J}_i^z(\omega) = \frac{g_v\varepsilon\tau_{ss}^z}{2\pi\nu}\left[\imath\nu\epsilon_{ij}\frac{\omega\tau}{\varepsilon\tau_{ss}^z}\frac{E_j(\omega)}{\left(1-2\imath\omega\tau\right)\left(1-\imath\omega\tau_{\parallel}\right)} - \frac{\mathcal{B}_i(\omega)}{1-\imath\omega\tau_{\parallel}}\right], \tag{35}$$

$$\mathcal{J}_i^i(\omega) = \frac{g_v\varepsilon\tau_{ss}^i}{2\pi\nu}\frac{\mathcal{B}_z(\omega)}{1-\imath\omega\tau_{\perp}}\,, \tag{36}$$

where the factor of $g_v = 2$ accounts for valley degeneracy. Furthermore, $\varepsilon_{zij}$ denotes the rank-3 Levi-Civita symbol, $\tau_{ss}^{i=x,y} = \tau_{ss}^z/2$ with $\tau_{ss}^z = 1/2\lambda$, and $\tau_{s,a}$ is the Dyakonov–Perel relaxation time introduced earlier [here, $\tau_{s,(x,y)} \equiv \tau_{\parallel}$ and $\tau_{s,z} \equiv \tau_{\perp} = \tau_{\parallel}/2$, with $\tau_{\parallel} = (4\lambda^2\tau)^{-1}$].

Equations (33)–(36) reveal several interesting features of the Dirac–Rashba model. First, a finite SHE is established in the presence of a time-dependent electric field (equation (35)). Second, a spin-injection field gives rise to a charge current (i.e. direct spin galvanic effect) (equation (33)) and a nonequilibrium spin polarization (equation (34)). Moreover, a pure spin current is induced by an applied spin-injection field (equations (35)–(36)). The induced spin-current density is polarized transversely to the spin-injection field. With the exception of the SHE, all such effects are present in the DC limit.

The linear response functions to external fields can be readily obtained from equations (33)–(36). For example, the optical conductivity $[\sigma_{ij}(\omega) = \delta J_i(\omega)/\delta E_j(\omega)]$, spin-galvanic susceptibility $[\chi_{ij}(\omega) = \delta S_i(\omega)/\delta E_j(\omega)]$ and spin Hall conductivity $[\sigma_{yx}^z(\omega) = \delta\mathcal{J}_y^z(\omega)/\delta E_x(\omega)]$ read as

$$\sigma_{ii}(\omega) = 2g_v\frac{\varepsilon\tau}{1-2\imath\omega\tau}\,, \qquad (\text{units of } e^2/h) \tag{37}$$

$$\chi_{ij}(\omega) \simeq -\frac{2g_v\epsilon_{ij}}{\nu}\frac{\lambda\tau}{1-\imath\omega\tau_{\parallel}}, \qquad (\text{units of } e/2\pi) \tag{38}$$

$$\sigma^z_{ij}(\omega) \simeq -\imath\epsilon_{ij}g_v\frac{\omega\tau}{1-\imath\omega\tau_{\parallel}}, \qquad (\text{units of } e/2\pi) \tag{39}$$

where subleading corrections of order $\omega\tau$ have been neglected for simplicity. These results deserve a few comments. The expression for $\sigma_{xx}(\omega)$ coincides with the familiar Drude model result, which is valid in the semiclassical regime with $\varepsilon\tau \gg 1$ [82]. More interestingly, the optical spin-galvanic susceptibility (equation (38)) generalizes the findings of [26] to an external electric field with nonzero frequency. Here, $\omega\tau_{\parallel}$ emerges as an important parameter that governs the imaginary part of the response function, whereas the physics of the DC regime reflects the average spin-precession angle experienced between consecutive scattering events (i.e. $\theta_p = \lambda\tau$).

## 3. Summary and outlook

We derived a quantum kinetic equation and the associated set of coupled spin–charge linear transport equations that govern the dynamics of Rashba-coupled 2D Dirac fermions in graphene proximitized by high-SOC materials. These equations, which are valid in the presence of arbitrary external fields, provide a quantitative description of rich interlinked spin–orbit scattering phenomena characteristic of 2D systems with broken inversion symmetry, including Dyakonov–Perel-type spin relaxation, direct and inverse DC spin-galvanic and optical spin Hall effects.

The distinctive feature of the SO(5) algebraic approach formulated in this work is that the exact large distance and long time behavior of the linear response one-particle density matrix, and thus also the expectation value of any local observable, is uniquely determined by a generalized *inverse diffuson* matrix (i.e. a *diffuson* Hamiltonian) that spans the full vector space of a 16-dimensional Clifford algebra. This is to be contrasted with the familiar SU(2) approach for two-dimensional electron gases [50, 83], whose Fourier-space *diffuson* operators are $4 \times 4$ matrices restricted to the space of charge and spin-polarization densities. The enlarged $(16 \times 16)$ *diffuson* Hamiltonian derived here emphasizes the manifestation of entanglement between the spin and pseudospin (sublattice) degrees of freedom that is ubiquitous across van der Waals materials. Furthermore, it provides direct access to the time evolution of all thermodynamic macroscopic observables, including spin-current density, spin-polarization density and sublattice-staggered densities.

This work opens up a number of avenues that can be explored in the framework introduced here. These range from the exploration of nonequilibrium opto-spintronic phenomena in group-VI dichalcogenide monolayers and van der Waals heterostructures with sizable spin–valley coupling, to the role played by spin–orbit-active impurities in spin dynamics and spin–charge conversion effects. In particular, asymmetric scattering precession [56] and skew scattering effects can be systematically explored by means of a nonperturbative $T$-matrix ladder scheme that resums all single-impurity scattering diagrams [26, 37, 39]. Such an extension of our diagrammatic treatment would be helpful in understanding the emergent transport physics of 2D van der Waals materials with broken sublattice symmetry, where the presence of non-coplanar $\mathbf{k}$-space spin textures at low energies is known to enable robust spin Hall effects irrespective of the type of impurities [36, 38], in addition to strongly modifying the spin dynamics [34, 35]. Moreover, our formalism could be employed to investigate how proximity-induced SOC affects the nonlocal resistance in Hanle-type spin precession experiments beyond its impact on the spin lifetimes. This could be examined by deriving a generalized spin diffusion equation accounting for the interplay of spin-valley coupling, intervalley scattering and the Bychkov-Rashba effect.

## Data availability statement

No new data were created or analysed in this study. This publication is theoretical work that does not require supporting research data.

## Acknowledgment

The author thanks D Perkins for proofreading the final version of the manuscript. This work was funded by the Royal Society through a Royal Society University Research Fellowship (Grant No. URF\R\191021).

## Appendix

The *diffuson* Hamiltonian in the standard weak SOC regime with $\epsilon\tau \gg 1$ reads as

$$\mathcal{H}_{\mathcal{D}}(\mathbf{q},\omega) = \imath\omega Q - \imath P\cdot\mathbf{q} + L \simeq \frac{1}{\tau}\begin{pmatrix} \begin{pmatrix} \mathcal{A}_{11} & \mathcal{A}_{12} \\ \mathcal{A}_{12} & \mathcal{A}_{22} \end{pmatrix} & \begin{pmatrix} \mathcal{C}_{11} & \mathbb{O} \\ \mathcal{C}_{21} & \mathbb{O} \end{pmatrix} \\ \begin{pmatrix} \mathcal{C}_{11} & -\mathcal{C}_{21} \\ \mathbb{O} & \mathbb{O} \end{pmatrix} & \begin{pmatrix} \mathcal{B}_{11} & \mathbb{O} \\ \mathbb{O} & \mathcal{B}_{22} \end{pmatrix} \end{pmatrix}, \tag{40}$$

where $\mathbb{O}$ is the null matrix, $\mathcal{A}_{11} = -\imath\omega\tau\,\mathbb{I}$,

$$\mathcal{A}_{12} = \begin{pmatrix} \imath v q_x\tau & 0 & 0 & 0 \\ 0 & \imath v q_x\tau & 0 & -2\lambda\tau \\ 0 & 0 & \imath v q_x\tau & 0 \\ 0 & 2\lambda\tau & 0 & \imath v q_x\tau \end{pmatrix}, \tag{41}$$

$$\mathcal{A}_{22} = \begin{pmatrix} 1-2\imath\omega\tau & 0 & 0 & 0 \\ 0 & 1-2\imath\omega\tau & 0 & 2\imath v q_x\lambda\tau^2 \\ 0 & 0 & 1-2\imath\omega\tau & 2\imath v q_y\lambda\tau^2 \\ 0 & -2\imath v q_x\lambda\tau^2 & -2\imath v q_y\lambda\tau^2 & 1-2\imath\omega\tau \end{pmatrix}, \tag{42}$$

$$\mathcal{B}_{11} = \begin{pmatrix} 1-2\imath\omega\tau & 0 & 0 & 0 \\ 0 & 1-2\imath\omega\tau & 0 & 2\imath v q_x\lambda\tau^2 \\ 0 & 0 & 1-2\imath\omega\tau & 2\imath v q_y\lambda\tau^2 \\ 0 & -2\imath v q_x\lambda\tau^2 & -2\imath v q_y\lambda\tau^2 & 1-2\imath\omega\tau \end{pmatrix}, \tag{43}$$

$$\mathcal{C}_{11} = \begin{pmatrix} \imath v q_y\tau & 0 & 0 & 0 \\ 0 & \imath v q_y\tau & 0 & 0 \\ 0 & 0 & \imath v q_y\tau & -2\lambda\tau \\ 0 & 0 & 2\lambda\tau & \imath v q_y\tau \end{pmatrix}, \tag{44}$$

$$\mathcal{C}_{21} = \begin{pmatrix} 0 & 0 & 0 & -\frac{4\lambda^2\tau}{\varepsilon} \\ 0 & 0 & -2\tau^2\lambda^2 & 0 \\ 0 & 2\tau^2\lambda^2 & 0 & 0 \\ -\frac{4\lambda^2\tau}{\varepsilon} & 0 & 0 & 0 \end{pmatrix}, \tag{45}$$

and $\mathcal{B}_{22} = [-\pi\varepsilon\tau/\ln(v\Lambda/\varepsilon) + \imath\pi^2\tau\omega/(4\ln^2(v\Lambda/\varepsilon))]\,\mathbb{I}$. Here, $\mathbb{I}$ denotes the $4\times 4$ identity matrix and $\Lambda$ is a momentum cutoff used to regularize the integrals in equation (19).

## ORCID iD

Aires Ferreira https://orcid.org/0000-0001-6017-8669

## References

[1] Manchon A, Železný J, Miron I M, Jungwirth T, Sinova J, Thiaville A, Garello K and Gambardella P 2019 Current-induced spin-orbit torques in ferromagnetic and antiferromagnetic systems *Rev. Mod. Phys.* **91** 035004
[2] Hellman F *et al* 2017 Interface-induced phenomena in magnetism *Rev. Mod. Phys.* **89** 025006
[3] Avsar A, Ochoa H, Guinea F, Özyilmaz B, van Wees B J and Vera-Marun I J 2020 *Colloquium*: spintronics in graphene and other two-dimensional materials *Rev. Mod. Phys.* **92** 021003
[4] Sierra J F, Fabian J, Kawakami R K, Roche S and Valenzuela S O 2021 Van der waals heterostructures for spintronics and opto-spintronics *Nat. Nanotechnol.* **16** 856–68
[5] Tombros N, Jozsa C, Popinciuc M, Jonkman H T and van Wees B J 2007 Electronic spin transport and spin precession in single graphene layers at room temperature *Nature* **448** 571–4
[6] Han W and Kawakami R K 2011 Spin relaxation in single-layer and bilayer graphene *Phys. Rev. Lett.* **107** 047207
[7] Zomer P J, Guimarães M H D, Tombros N and van Wees B J 2012 Long-distance spin transport in high-mobility graphene on hexagonal boron nitride *Phys. Rev.* B **86** 161416

[8] Venkata Kamalakar M, Groenveld C, Dankert Ae and Dash S P 2015 Long distance spin communication in chemical vapour deposited graphene *Nat. Commun.* **6** 6766
[9] Yan W *et al* 2016 Long spin diffusion length in few-layer graphene flakes *Phys. Rev. Lett.* **117** 147201
[10] Gebeyehu Z M *et al* 2019 Spin communication over 30 $\mu$m long channels of chemical vapor deposited graphene on $SiO_2$ *2D Mater.* **6** 034003
[11] Sepioni M, Nair R R, Rablen S, Narayanan J, Tuna F, Winpenny R, Geim A K and Grigorieva I V 2010 Limits on intrinsic magnetism in graphene *Phys. Rev. Lett.* **105** 207205
[12] Sichau J, Prada M, Anlauf T, Lyon T J, Bosnjak B, Tiemann L and Blick R H 2019 Resonance microwave measurements of an intrinsic spin-orbit coupling gap in graphene: a possible indication of a topological state *Phys. Rev. Lett.* **122** 046403
[13] Ferreira A, Rappoport T G, Cazalilla M A and Castro Neto A H 2014 Extrinsic spin Hall effect induced by resonant skew scattering in graphene *Phys. Rev. Lett.* **112** 066601
[14] Balakrishnan J *et al* 2014 Giant spin Hall effect in graphene grown by chemical vapour deposition *Nat. Commun.* **5** 4748
[15] Avsar A *et al* 2014 Spin–orbit proximity effect in graphene *Nat. Commun.* **5** 4875
[16] Wang Z, Ki D-K, Chen H, Berger H, MacDonald A H and Morpurgo A F 2015 Strong interface-induced spin–orbit interaction in graphene on $WS_2$ *Nat. Commun.* **6** 8339
[17] Wang Z, Ki D-K, Khoo J Y, Mauro D, Berger H, Levitov L S and Morpurgo A F 2016 Origin and magnitude of 'designer' spin-orbit interaction in graphene on semiconducting transition metal dichalcogenides *Phys. Rev.* X **6** 041020
[18] Gmitra M, Kochan D, Högl P and Fabian J 2016 Trivial and inverted Dirac bands and the emergence of quantum spin Hall states in graphene on transition-metal dichalcogenides *Phys. Rev.* B **93** 155104
[19] Island J O *et al* 2019 Spin–orbit-driven band inversion in bilayer graphene by the van der Waals proximity effect *Nature* **571** 85–9
[20] Yang B, Tu M-F, Kim J, Wu Y, Wang H, Alicea J, Wu R, Bockrath M and Shi J 2016 Tunable spin–orbit coupling and symmetry-protected edge states in graphene/$WS_2$ *2D Mater.* **3** 031012
[21] Yang B *et al* 2017 Strong electron-hole symmetric Rashba spin-orbit coupling in graphene/monolayer transition metal dichalcogenide heterostructures *Phys. Rev.* B **96** 041409
[22] Völkl T, Rockinger T, Drienovsky M, Watanabe K, Taniguchi T, Weiss D and Eroms J 2017 Magnetotransport in heterostructures of transition metal dichalcogenides and graphene *Phys. Rev.* B **96** 125405
[23] Zihlmann S, Cummings A W, Garcia J H, Kedves Mé, Watanabe K, Taniguchi T, Schönenberger C and Makk P 2018 Large spin relaxation anisotropy and valley-Zeeman spin-orbit coupling in $WSe_2$/graphene/*h*-BN heterostructures *Phys. Rev.* B **97** 075434
[24] Wakamura T, Reale F, Palczynski P, Guéron S, Mattevi C and Bouchiat H 2018 Strong anisotropic spin-orbit interaction induced in graphene by monolayer $ws_2$ *Phys. Rev. Lett.* **120** 106802
[25] Rashba E I 2009 Graphene with structure-induced spin-orbit coupling: spin-polarized states, spin zero modes and quantum Hall effect *Phys. Rev.* B **79** 161409
[26] Offidani M, Milletarì M, Raimondi R and Ferreira A 2017 Optimal charge-to-spin conversion in graphene on transition-metal dichalcogenides *Phys. Rev. Lett.* **119** 196801
[27] Ghiasi T S, Kaverzin A A, Blah P J and van Wees B J 2019 Charge-to-spin conversion by the Rashba–Edelstein effect in two-dimensional van der Waals heterostructures up to room temperature *Nano Lett.* **19** 5959–66
[28] Antonio Benítez L, Torres W S, Sierra J F, Timmermans M, Garcia J H, Roche S, Costache M V and Valenzuela S O 2020 Tunable room-temperature spin galvanic and spin Hall effects in van der Waals heterostructures *Nat. Mater.* **19** 170–5
[29] Li L *et al* 05 2020 Gate-tunable reversible Rashba–Edelstein effect in a few-layer graphene/2H-$TaS_2$ heterostructure at room temperature *ACS Nano* **14** 5251–9
[30] Hoque A Md, Khokhriakov D, Zollner K, Zhao B, Karpiak B, Fabian J and Dash S P 2021 All-electrical creation and control of spin-galvanic signal in graphene and molybdenum ditelluride heterostructures at room temperature *Commun. Phys.* **4** 124
[31] Kondou K, Yoshimi R, Tsukazaki A, Fukuma Y, Matsuno J, Takahashi K S, Kawasaki M, Tokura Y and Otani Y 2016 Fermi-level-dependent charge-to-spin current conversion by Dirac surface states of topological insulators *Nat. Phys.* **12** 1027–31
[32] Ghiasi T S, Ingla-Aynés J, Kaverzin A A and van Wees B J 2017 Large proximity-induced spin lifetime anisotropy in transition-metal dichalcogenide/graphene heterostructures *Nano Lett.* **17** 7528–32
[33] Antonio Benítez L, Sierra J F, Torres W S, Arrighi A, Bonell Fedéric, Costache M V and Valenzuela S O 2017 Strongly anisotropic spin relaxation in graphene–transition metal dichalcogenide heterostructures at room temperature *Nat. Phys.* **14** 303–8
[34] Cummings A W, Garcia J H, Fabian J and Roche S 2017 Giant spin lifetime anisotropy in graphene induced by proximity effects *Phys. Rev. Lett.* **119** 206601
[35] Offidani M and Ferreira A 2018 Microscopic theory of spin relaxation anisotropy in graphene with proximity-induced spin-orbit coupling *Phys. Rev.* B **98** 245408
[36] Milletarì M, Offidani M, Ferreira A and Raimondi R 2017 Covariant conservation laws and the spin Hall effect in Dirac–Rashba systems *Phys. Rev. Lett.* **119** 246801
[37] Offidani M, Raimondi R and Ferreira A 2018 Microscopic linear response theory of spin relaxation and relativistic transport phenomena in graphene *Condens. Matter* **3** 18
[38] Offidani M and Ferreira A 2018 Anomalous Hall effect in 2D Dirac materials *Phys. Rev. Lett.* **121** 126802
[39] Sousa F, Tatara G and Ferreira A 2020 Skew-scattering-induced giant antidamping spin-orbit torques: collinear and out-of-plane Edelstein effects at two-dimensional material/ferromagnet interfaces *Phys. Rev. Res.* **2** 043401
[40] Cavill S A, Huang C, Offidani M, Lin Y-H, Cazalilla M A and Ferreira A 2020 Proposal for unambiguous electrical detection of spin-charge conversion in lateral spin valves *Phys. Rev. Lett.* **124** 236803
[41] Hirsch J E 1999 Spin Hall effect *Phys. Rev. Lett.* **83** 1834–7
[42] Garcia J H, Vila M, Cummings A W and Roche S 2018 Spin transport in graphene/transition metal dichalcogenide heterostructures *Chem. Soc. Rev.* **47** 3359–79
[43] Joao S M, Andelkovic M, Covaci L, Rappoport T G, Lopes J M V P and Ferreira A 2020 Kite: high-performance accurate modelling of electronic structure and response functions of large molecules, disordered crystals and heterostructures *R. Soc. Open Sci.* **7** 191809
[44] Van Tuan D, Marmolejo-Tejada J M, Waintal X, Nikolić B K, Valenzuela S O and Roche S 2016 Spin Hall effect and origins of nonlocal resistance in adatom-decorated graphene *Phys. Rev. Lett.* **117** 176602
[45] Schaibley J R, Yu H, Clark G, Rivera P, Ross J S, Seyler K L, Yao W and Xu X 2016 Valleytronics in 2D materials *Nat. Rev. Mater.* **1** 16055
[46] Xiao Di, Liu G-B, Feng W, Xu X and Yao W 2012 Coupled spin and valley physics in monolayers of $MoS_2$ and other group-VI dichalcogenides *Phys. Rev. Lett.* **108** 196802

[47] Luo Y K, Xu J, Zhu T, Wu G, McCormick E J, Zhan W, Neupane M R and Kawakami R K 2017 Opto-valleytronic spin injection in monolayer $MoS_2$/few-layer graphene hybrid spin valves *Nano Lett.* **17** 3877–83

[48] Avsar A, Unuchek D, Liu J, Sanchez O L, Watanabe K, Taniguchi T, Özyilmaz B and Kis A 2017 Optospintronics in graphene via proximity coupling *ACS Nano* **11** 11678–86

[49] Zhang P and Wu M W 2011 Electron spin diffusion and transport in graphene *Phys. Rev.* B **84** 045304

[50] Burkov A A, Núñez A S and MacDonald A H 2004 Theory of spin-charge-coupled transport in a two-dimensional electron gas with Rashba spin-orbit interactions *Phys. Rev.* B **70** 155308

[51] Wenk P and Kettemann S 2010 Dimensional dependence of weak localization corrections and spin relaxation in quantum wires with Rashba spin-orbit coupling *Phys. Rev.* B **81** 125309

[52] Bychkov Y A and Rashba E I 1984 Properties of a 2D electron gas with lifted spectral degeneracy *JETP Lett.* **39**

[53] Within the single-valley representation adopted in this work, the Pauli matrices $\sigma_a$ and $s_b$ all anticommute with $\mathcal{T}$, so that their products are invariant under the time-reversal operation. The Hamiltonian at the $K'$ point is obtained by simply changing the sign of the time-like gauge-field component $\mathcal{A}^0_K = -\mathcal{A}^0_{K'} = \lambda_{\rm sv} s_z$, known in the literature as valley-Zeeman interaction or spin-valley coupling

[54] Pachoud A, Ferreira A, Özyilmaz B and Neto A H C 2014 Scattering theory of spin-orbit active adatoms on graphene *Phys. Rev.* B **90** 035444

[55] Yang H-Y, Huang C, Ochoa H and Cazalilla M A 2016 Extrinsic spin Hall effect from anisotropic Rashba spin-orbit coupling in graphene *Phys. Rev.* B **93** 085418

[56] Huang C, Chong Y D and Cazalilla M A 2016 Direct coupling between charge current and spin polarization by extrinsic mechanisms in graphene *Phys. Rev.* B **94** 085414

[57] Milletarì M and Ferreira A 2016 Quantum diagrammatic theory of the extrinsic spin Hall effect in graphene *Phys. Rev.* B **94** 134202

[58] Milletarì M and Ferreira A 2016 Crossover to the anomalous quantum regime in the extrinsic spin Hall effect of graphene *Phys. Rev.* B **94** 201402

[59] Žutić I, Fabian J and Das Sarma S 2004 Spintronics: fundamentals and applications *Rev. Mod. Phys.* **76** 323–410

[60] Wu M W, Jiang J H and Weng M Q 2010 Spin dynamics in semiconductors *Phys. Rep.* **493** 61–236

[61] Boross Peter, Dóra Bazs, Kiss Aaria and Simon F 2013 A unified theory of spin-relaxation due to spin-orbit coupling in metals and semiconductors *Sci. Rep.* **3** 3233

[62] Raes B, Scheerder J E, Costache M V, Bonell Fedéric, Sierra J F, Cuppens J, Van de Vondel J and Valenzuela S O 2016 Determination of the spin-lifetime anisotropy in graphene using oblique spin precession *Nat. Commun.* **7** 11444

[63] Ringer S, Hartl S, Rosenauer M, Völkl T, Kadur M, Hopperdietzel F, Weiss D and Eroms J 2018 Measuring anisotropic spin relaxation in graphene *Phys. Rev.* B **97** 205439

[64] Fetter A L and Walecka J D 1971 *Quantum Theory of Many-Particle Systems* (Boston: McGraw-Hill)

[65] Doniach S and Sondheimer E H 1998 *Green's Functions for Solid State Physicists* (London: Imperial College Press)

[66] Mahan G D 2000 *Many Particle Physics* 3rd edn (New York: Plenum)

[67] Ado I A, Dmitriev I A, Ostrovsky P M and Titov M 2015 Anomalous Hall effect with massive Dirac fermions *Europhys. Lett.* **111** 37004

[68] This is markdly different in models with noncoplanar spin texture, e.g. caused by the interplay of BR effect and spin-valley coupling. The resulting net $\hat{z}$-spin polarization at each valley activates a robust skew scattering mechanism, whose description relies on high-order scattering processes that are best described within the T-matrix framework [36, 37]. A detailed discussion on the validity of the Gaussian approximation for 2D Dirac fermions is given in [57].

[69] Shen K, Raimondi R and Vignale G 2014 Theory of coupled spin-charge transport due to spin-orbit interaction in inhomogeneous two-dimensional electron liquids *Phys. Rev.* B **90** 245302

[70] Burkov A A and Hawthorn D G 2010 Spin and charge transport on the surface of a topological insulator *Phys. Rev. Lett.* **105** 066802

[71] Sacksteder V E, Kettemann S, Wu Q, Dai Xi and Fang Z 2012 Spin conduction in anisotropic three-dimensional topological insulators *Phys. Rev.* B **85** 205303

[72] Basko D M 2008 Theory of resonant multiphonon Raman scattering in graphene *Phys. Rev.* B **78** 125418

[73] Schliemann J 2017 *Colloquium*: persistent spin textures in semiconductor nanostructures *Rev. Mod. Phys.* **89** 011001

[74] Cysne T P, Ferreira A and Rappoport T G 2018 Crystal-field effects in graphene with interface-induced spin-orbit coupling *Phys. Rev.* B **98** 045407

[75] Shen K, Vignale G and Raimondi R 2014 Microscopic theory of the inverse Edelstein effect *Phys. Rev. Lett.* **112** 096601

[76] In the absence of intervalley scattering channels (i.e., for scalar impurities), the transport time of 2D Dirac fermions is twice the scattering time $\tau_{\rm tr} = 2\tau$ due to the suppression of backscattering events.

[77] Kato Y K, Myers R C, Gossard A C and Awschalom D D 2004 Observation of the spin Hall effect in semiconductors *Science* **306** 1910–13

[78] Wunderlich J, Kaestner B, Sinova J and Jungwirth T 2005 Experimental observation of the spin-Hall effect in a two-dimensional spin-orbit coupled semiconductor system *Phys. Rev. Lett.* **94** 047204

[79] Dimitrova O'ga V 2005 Spin-hall conductivity in a two-dimensional Rashba electron gas *Phys. Rev.* B **71** 245327

[80] Aranov A G and Lyanda-Geller Y B 1989 Spin polarization of electrons by an electric current *JETP Lett.* **50** 431

[81] Edelstein V M 1990 Spin polarization of conduction electrons induced by electric current in two-dimensional asymmetric electron systems *Solid State Commun.* **73** 233–5

[82] Bludov Y V, Ferreira A, Peres N M R and Vasilevskiy M I 2013 A primer on surface plasmon-polaritons in graphene *Int. J. Mod. Phys.* B **27** 1341001

[83] Shen K, Raimondi R and Vignale G 2014 Theory of coupled spin-charge transport due to spin-orbit interaction in inhomogeneous two-dimensional electron liquids *Phys. Rev.* B **90** 245302